

Key Structural Transformations and Kinetics of Pt Nanoparticles in PEFC Pt/C Electrocatalysts by a Simultaneous Operando Time-Resolved QXAFS XRD Technique

著者 (英)	Oki Sekizawa, Takuma Kaneko, Kotaro Higashi, Shinobu Takao, Yusuke Yoshida, Takao Gunji, Xiao Zhao, Gabor Samjeske, Tomohiro Sakata, Tomoya Uruga, Yasuhiro Iwasawa
journal or publication title	Topics in Catalysis
volume	61
number	9-11
page range	889-901
year	2018-06
URL	http://id.nii.ac.jp/1438/00009281/

doi: 10.1007/s11244-018-0934-1

Key Structural Transformations and Kinetics of Pt Nanoparticles in PEFC Pt/C Electrocatalysts by a Simultaneous Operando Time-Resolved QXAFS–XRD Technique

Short Title:

Structural Transformations and Kinetics of Pt Nanoparticles in PEFC Pt/C

Oki Sekizawa,^{a,b} Takuma Kaneko,^a Kotaro Higashi,^a Shinobu Takao,^a Yusuke Yoshida,^a Takao Gunji,^a Xiao Zhao,^a Gabor Samjeské,^a Tomohiro Sakata,^a Tomoya Uruga,^{a,b} and Yasuhiro Iwasawa^{a,c*}

^a Innovation Research Center for Fuel Cells, The University of Electro-Communications, Chofugaoka, Chofu, Tokyo 182-8585, Japan

^b Japan Synchrotron Radiation Research Institute, Spring-8, Sayo, Hyogo 679-5198, Japan

^c Department of Engineering Science, Graduate School of Informatics and Engineering, The University of Electro-Communications, Chofugaoka, Chofu, Tokyo 182-8585, Japan

Abstract

This account article treats with the key structural transformations and kinetics of Pt nanoparticles in Pt/C cathode catalysts under transient voltage operations ($0.4 V_{RHE} \rightarrow 1.4 V_{RHE} \rightarrow 0.4 V_{RHE}$) by simultaneous operando time-resolved QXAFS–XRD measurements, summarizing and analyzing our previous kinetic data in more detail and discussing on the key reaction steps and rate constants for the performance and durability of polymer electrolyte fuel cells (PEFC). The time-resolved QXAFS–XRD measurements were conducted at each acquisition time of 20 ms, while measuring the current/charge of the PEFC. The rate constants for the transient responses of Pt valence, CN(Pt–O) (CN: coordination number), CN(Pt–Pt), and Pt metallic-phase core size under the transient voltage operations were determined by the combined time-resolved QXAFS–XRD technique. The relationship of the structural kinetics with the performance and durability of the PEFC Pt/C was also documented as key issues for the development of next-generation PEFCs. The present account emphasizes the time-resolved QXAFS and XRD techniques to be a powerful technique to analyze directly the structural and electronic change of metal nanoparticles inside PEFC under the operating conditions.

Keywords: Simultaneous *operando* time-resolved QXAFS–XRD measurements, Pt/C cathode catalyst, Polymer electrolyte fuel cell, Mechanism and structural kinetics, Performance and durability.

1. Introduction

Polymer electrolyte fuel cell (PEFC), which can bring zero emission vehicles into reality in the future due to high power density and efficiency at low temperatures,

has extensively been studied thus far. Nevertheless, improvements of the oxygen reduction reaction (ORR) activity and durability of Pt/C cathode catalysts in membrane electrode assembly (MEA) of PEFC to

remarkably reduce the Pt amount and PEFC stacking cost are still indispensable.[1-11] To develop next-generation PEFCs for automobiles, the molecular-level structural kinetics and dynamic behaviors of cathode catalysts under the harsh PEFC operating conditions must be understood more thoroughly. However, it is hard to elucidate the dynamic transformation of Pt nanoparticles in the MEA because there are few suitable *in situ* analysis methods for direct observation of Pt nanoparticles of Pt/C cathode layer inside the MEA with a stacking structure in PEFC.

Time-resolved quick X-ray absorption fine structure (QXAFS) enables *in situ* element-selective investigation on the dynamic transformations of the local structures and oxidation states of Pt nanoparticles in Pt/C cathode catalysts during the electrochemical reactions at the Pt surface under the PEFC operating conditions,[11-17] while time-resolved X-ray diffraction (XRD) enables *in situ* measurements of dynamic transformations of the crystalline structure of the metallic-phase core of Pt electrocatalysts.[18-20] Recently, we designed a combined system for simultaneous time-resolved measurements of QXAFS and XRD of MEA cathode catalysts and reported the first example of simultaneous *operando* time-resolved QXAFS–XRD measurements at each acquisition time of 20 ms to evidence the dynamic structural and electronic behavior of an MEA Pt/C cathode catalyst under the transient cyclic voltage operations $0.4 V_{\text{RHE}} \rightarrow 1.4 V_{\text{RHE}} \rightarrow 0.4 V_{\text{RHE}}$ (vs RHE).[21] We also reported the structural kinetics controlling the ORR activity and reflecting the durability of the Pt/C cathode catalysts by the systematic series of QXAFS analysis.[22]

In this account we document the application of the simultaneous time-resolved QXAFS-XRD technique to a PEFC Pt/C cathode catalyst, re-analysing our

previous structural kinetics data under the transient voltage operation $1.4 V_{\text{RHE}} \rightarrow 0.4 V_{\text{RHE}}$ in more detail, and the direct information on the key structural kinetics relevant to the performance and durability of different Pt/C catalysts by the time-resolved QXAFS method for thorough understanding of the cathode catalysis toward PEFC improvement.

2. Experimental

2.1 MEA preparations and electrochemical measurements

The MEA cathode catalysts, electrochemical measurements, QXAFS experiments and data analysis, and rate constant decision are described previously in detail [21,22], but briefly described below. A cathode catalyst was Pt/C (Pt 46.1 wt%, TEC10E50E, Tanaka Kikinzoku Kogyo; surface area: $385 \text{ m}^2/\text{g}$), and Ru/C (Ru 30 wt%, TECRu(ONLY)E50, Tanaka Kikinzoku Kogyo) was used as an anode catalyst to avoid interference against XAFS measurements of the Pt/C cathode. The MEAs were provided by Eiwa Co. Ltd., Japan, which constitutes an anode layer, a Nafion® NR-212 membrane (Sigma-10 Aldrich) and a cathode layer. The size of the MEA was $3.0 \times 3.3 \text{ cm}$, and catalyst loadings at the cathode and anode were $0.6 \text{ mg-Pt/Ru cm}^{-2}$. The prepared MEAs were sandwiched in a home-made XAFS cell using Viton® gaskets of 0.15 mm thickness, gas diffusion layers (GDL:TGP-H-060 (10wt% PTFE treatment)) and separator-plates (bipolar plates) with serpentine-shape type flow channels for both anode and cathode sides. The average particle size in the fresh (activated) Pt/C catalyst in MEA was estimated to be $2.6 \pm 0.9 \text{ nm}$ by the analysis of TEM images.

The cathode was connected as working electrode and the anode (hydrogen-fed) served as combined counter and reference electrode. All potentials are referred to this pseudo hydrogen reference electrode

(RHE). The gas flows of H₂ (99.99999%; 100 sccm) for anode and N₂ (99.99995%; 600 sccm) or air (99.99995%; 900 sccm) for cathode were regulated by mass-flow controllers and were bubbled through humidifiers at 351 K. The humidified gases were supplied to the *in situ* XAFS cell heated at 353 K, resulting in ~ 93% relative humidity (RH). The MEAs in the XAFS cell were conditioned by 150 aging cycles with a sequence of step-wise galvanostatic current steps every 6 s from open circuit voltage (OCV) to a potential near 0.3 V_{RHE} in H₂ (anode) and air (cathode) operating atmospheres. Cyclic voltammograms (CVs) and I-V loads were measured after the aging treatment. The CV measurements in *in situ* PEFC conditions were conducted between 0.05 and 0.9 V_{RHE} at 20 mV s⁻¹ in H₂ (anode) and N₂ (cathode) operating atmospheres. The cell voltage was controlled using a potentiostat-galvanostat (Autolab PGSTAT302N, Metrohm, Netherlands) and current amplifier (Autolab BOOSTER20A, Metrohm).

Besides the Pt/C (C: Ketjenblack(KB); TEC10E50E), other two kinds of Pt/C cathode catalysts, Pt/Acetylene black(AB) (surface area: 437 m²/g) and Pt/multi-walled carbon nanotube (MWCNT) (surface area: 182 m²/g) provided by a manufacturer were also used to study the relationship between the rate constants for the elementary steps and the performance and durability of the MEA Pt/C. The cathode degradation was carried out by accelerated durability test (ADT) cycles with a triangular wave between 1.0 and 1.5 V_{RHE} at 0.5 V s⁻¹ in H₂ (anode) and N₂ (cathode) operating atmospheres. Cyclic voltammograms (CVs) and I-V loads were measured after the aging treatment and ADT cycles. The electrochemical surface areas (ECSAs) of the cathode catalysts in MEAs at 353K were calculated by charge density of H₂ adsorption on a Pt surface (210 μC/cm²-Pt²) in the H₂

underpotential deposition region (0.05 V– ca. 0.4 V of the onset of the double-layer region). [23]

2.2 *In situ* time-resolved XAFS and XRD measurements

The series of *in situ* time-resolved Pt L_{III}-edge XAFS spectra and *in situ* time-resolved XRD patterns for Pt/C in MEA under the transient voltage operations (anode: H₂; cathode: N₂; 353 K; ~93% relative humidity) were measured at BL36XU station in SPring-8, which was constructed by our group.[24] The QXAFS spectra were measured in a transmission mode by using a Si(111) channel-cut monochromator on a high-speed galvano scanner, and using high-speed ion chambers (S1196D1, OKEN). The PEFC cell was placed between I₀ ion chamber (Ar 15%/N₂ 85%) and I₁ ion chamber (Ar 50%/N₂ 50%), and Pt foil was placed between I₁ ion chamber and I₂ ion chamber (Ar 50%/N₂ 50%) for energy calibration.

The cell voltage was changed from the open-circuit voltage (OCV) to 0.4 V_{RHE}, where the voltage was kept for 300 s, followed by the rapid voltage jump from 0.4 V_{RHE} to 1.4 V_{RHE} (at time=zero for the transient voltage up process), and this voltage was kept for 300 s, and then reversely, the cell voltage was jumped rapidly from 1.4 V_{RHE} to 0.4 V_{RHE} (at time=zero for the transient voltage down process). The transient responses of the MEA cathode catalysts against the cycling voltage operations were measured by time-resolved QXAFS at a time resolution of 20 ms for 30 s from 10 s before each voltage jump.[21]

In situ time-resolved XRD measurements were conducted every 20 ms (acquisition time: 17 ms, read out time: 3 ms) at an incidence X-ray energy of 12,638 eV in the 2θ range of 20 – 45° using a high-speed 2D detector ((PILATUS 300K-W, DECTRIS),

while measuring the current/charge of PEFC during the potential operating processes. The transient responses of the MEA cathode catalysts against the voltage cycling operations for 30 s from 10 s before each voltage jump were also measured by the *in situ* time-resolved XRD technique using a 24bit ADC (analog digital converter; PXI-5922) for PILATUS signals and a TTL trigger of a potentiostat for time-resolved XRD measurement.[21]

In the study on the relationship between the rate constants under the transient cyclic voltage operations and the performance and durability of the MEA Pt/C cathode catalysts, the transient responses of the MEA cathode catalysts against the cycling voltage operations were measured by QXAFS at a time resolution of 100 ms for 30 s from 10 s before each voltage jump.[22]

2.3 QXAFS and XRD analyses

QXANES and QEXAFS spectra were analyzed in the similar way to the previous reports,[11,14-17] using the Larch code (v0.9.20a) containing the IFEFFIT Package (Athena and Artemis).[25-27] The white line peaks of normalized QXANES spectra were analyzed by curve fitting with a Lorentzian function and an arctangent function. Background subtraction in QEXAFS analysis was performed using Autobk program.[28] The extracted k^3 -weighted Pt L_{III}-edge EXAFS oscillations were Fourier transformed into *R*-space over $k = 30\text{--}130\text{ nm}^{-1}$, and the curve fittings were performed in the *R*-space (0.12–0.31 nm). The fitting parameters for each shell were the coordination number (CN), interatomic distance (*R*), Debye–Waller factor (σ^2), and correction-of-edge energy (ΔE_0). The phase shifts and backscattering amplitude for each shell were calculated with FEFF8.5-Lite code using structural parameters obtained from the crystal structures of Pt and PtO₂. [29] Self-consistent field

potentials were added to the FEFF calculations for the reliable determination of the Fermi level. The amplitude reduction factor (S_0^2) for Pt-Pt bonds in this study was estimated to be 0.916 by analyzing Pt foil.

For the time-resolved XRD analysis we measured XRD patterns for a blank cell with a Nafion membrane and without catalyst layers and removed background signals by correcting the XRD data with a non-linear scale factor. XRD (220) diffraction peak was fitted by the pseudo-Voigt function and Pt particle sizes in MEA Pt/C cathode catalysts were calculated by the Scherrer equation.

2.4 Rate constant estimations

The white line peak height of the Pt L_{III}-edge QXANES, the coordination number (CN) of Pt-Pt and Pt-O, and the current/charge variation of PEFC MEA recorded on the electrochemical P/G stat were plotted against time in the transient response processes under the voltage operations $0.4\text{ V}_{\text{RHE}} \rightarrow 1.4\text{ V}_{\text{RHE}}$ and $1.4\text{ V}_{\text{RHE}} \rightarrow 0.4\text{ V}_{\text{RHE}}$. The integrated intensity of XRD (111) and (220) peaks was calculated by Gaussian function fitting. Pt metallic-phase size was calculated by the Scherrer equation ($K=1$) using integral width from the Gaussian function fitting of the (220) peak. The (111) peak intensity and (220) peak intensity and Pt metallic-phase size were also plotted against time in the transient response processes. The rate constants for the surface chemical reaction processes and Pt metallic-phase size change under the transient cyclic voltage operations $0.4\text{ V}_{\text{RHE}} \rightarrow 1.4\text{ V}_{\text{RHE}} \rightarrow 0.4\text{ V}_{\text{RHE}}$ were determined from the time profiles of the QXAFS and XRD analysis data. The rate constants determined from the time change in the above parameters were estimated by data fitting using an exponential function (eq. (1)) or a linear combination of two exponential functions (eq. (2)), taking into account

the error weighting given by the inverse of the error.[22] The data fitting with one or two exponential functions for the change of each parameter against time (t) was performed for the period of 0–20 s after the voltage was jumped ($0.4 V_{RHE} \rightarrow 1.4 V_{RHE}$ and $1.4 V_{RHE} \rightarrow 0.4 V_{RHE}$).

$$f(t)_{one} = y_0 + a_1 \exp(-k_1 t) \quad (1)$$

$$f(t)_{two} = y_0 + a_1 \exp(-k_1 t) + a_2 \exp(-k_2 t) \quad (2)$$

In eq. (1) and eq. (2) y_0 is an experimentally determined constant, and the parameters k_1 , k_2 , a_1 , a_2 and t are rate constants (k_1 and k_2), change amounts (a_1 and a_2) and reaction time (t) for fast and slow structural kinetics of the Pt/C in MEA. It is to be noted that the analysis of QXAFS and XRD data by exponential functions to determine the first-order rate constants is independent of Pt quantity and Pt utilization in MEAs and reflects the dynamic changes of the Pt valence and local coordination structure and the ordered crystalline structure in the transient response processes.[21,22]

3. Results and Discussion

3.1 Simultaneous time-resolved QXAFS–XRD measurement system and transient response profiles of Pt nanoparticles in MEA Pt/C under cyclic voltage operations

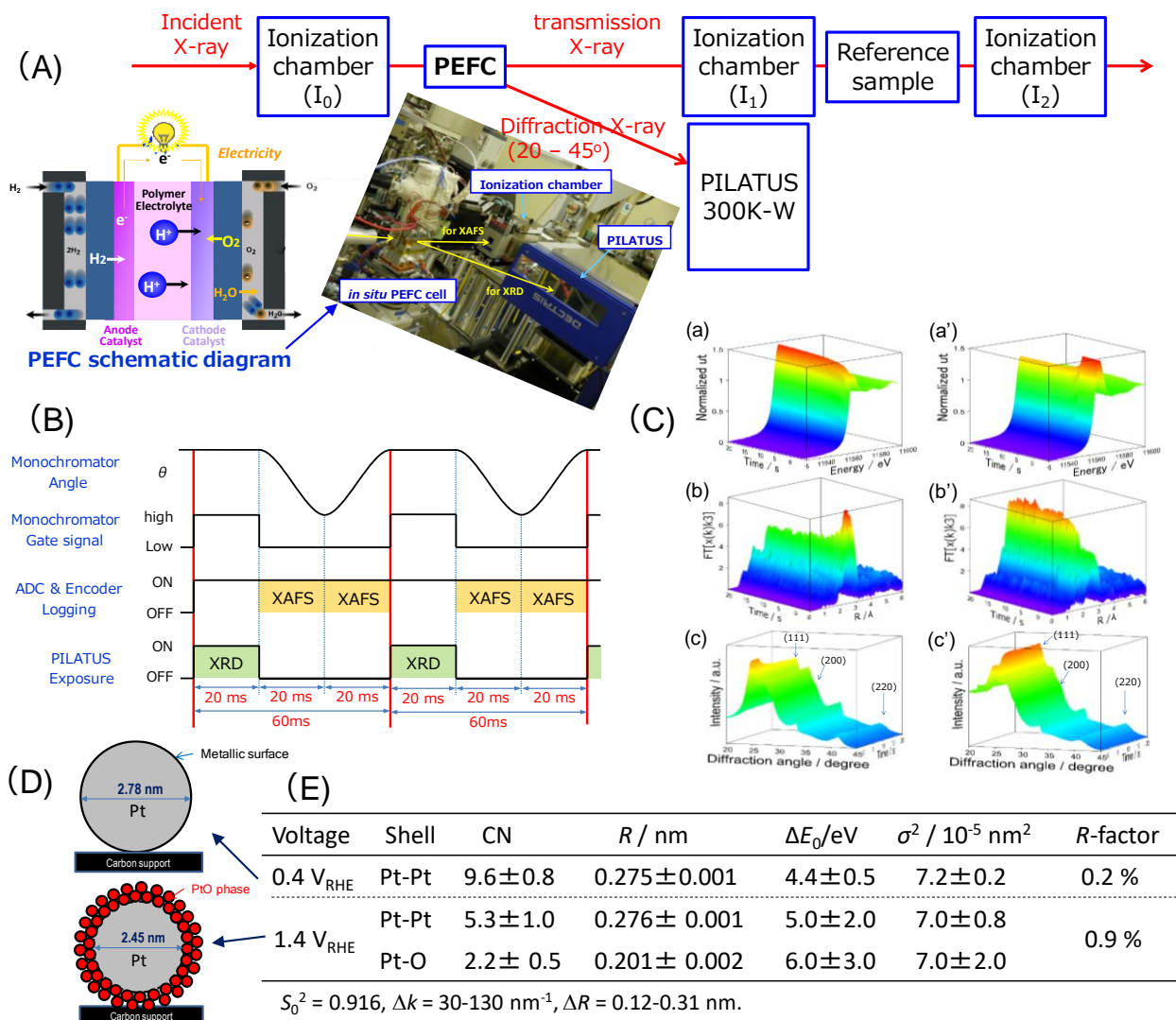
The simultaneous *operando* time-resolved QXAFS–XRD measurements for MEA Pt/C under transient voltage operations (anode: H_2 ; cathode: N_2) at 60 ms time-resolution (20 ms QXAFS x2 + 20 ms XRD x1 = 60 ms) were performed at SPring-8 BL36XU beamline, which we have developed.[24] The experimental setup for the simultaneous *operando* time-resolved measurements of QXAFS and XRD, while measuring the current/charge of PEFC is shown in Figure 1 (A), where a high-speed regulation pattern of monochromator angles for the simultaneous QXAFS–XRD measurements is also

shown in Figure 1 (B). The incident X-rays were irradiated to an MEA Pt/C cathode in an *in situ* PEFC cell at an angle of 10° to the MEA plane. The cell voltage was changed from the open-circuit voltage (OCV) to $0.4 V_{RHE}$, where the voltage was kept for 300 s, followed by the rapid voltage jump from $0.4 V_{RHE}$ to $1.4 V_{RHE}$, and this voltage was kept for 300 s, and then reversely the cell voltage was jumped rapidly from $1.4 V_{RHE}$ to $0.4 V_{RHE}$.

The *operando* time-resolved Pt L_{III} -edge QXAFS spectra and XRD patterns for an MEA Pt/C at 60 ms time resolution were successfully measured by the developed combined technique for the first time (Figure 1 (C)).[21] The typical structural parameters at $0.4 V_{RHE}$ and $1.4 V_{RHE}$ determined by the curve-fitting QEXAFS analysis are listed in Figure 1 (E). The Pt nanoparticle structures in the MEA Pt/C are also shown in Figure 1 (D) on the basis of the time-resolved QEXAFS, time-resolved XRD and TEM. For the cathode catalysts at $0.4 V_{RHE}$ only Pt–Pt bonds at 0.275 ± 0.001 nm were observed, indicating the metallic state of Pt nanoparticles on carbon. The CN (Pt–Pt) was 9.6 ± 0.8 . The Pt nanoparticles with $2.6 (\pm 0.9)$ nm dimension (TEM) are regarded to constitute approximately 5 Pt layers (the fifth, fourth, third, second, and first layers and a central atom), assuming sphere structures with the fcc arrangement (d_{111} (interplanar spacing) ~ 0.23 nm), and hence the CN(Pt–Pt) is estimated to be 10.6 by eq.(3),

$$CN(Pt-Pt) = \frac{12 \cdot (1^2 + 2^2 + 3^2 + 4^2) + 9 \cdot 5^2}{(1^2 + 2^2 + 3^2 + 4^2 + 5^2)} = 10.6 \quad (3),$$

where 12 is the CN of Pt atoms in fcc Pt bulk (1st–4th Pt layer) and 9 is the CN of Pt atoms at the outermost surface (5th Pt layer).[14] The observed CN(Pt–Pt) value is compatible with 10.6, taking into account the experimental error ranges in both XAFS and TEM. At



1.4 V_{RHE}, the Fourier transform of the QEXAFS data was fitted with two shells of Pt-Pt at 0.276 ± 0.001 nm and Pt-O at 0.201 ± 0.002 nm (Figure 1 (E)), indicating the oxidation of the Pt catalyst surface as reported previously for Pt/KB, Pt/AB, Pt/MWCNT, Pt₃Co/KB,

Pt₃Ni/KB, SnO₂/Pt/KB and SnO₂/Pt₃Co/KB.[7,11,14-17] The CN(Pt-Pt) and CN(Pt-O) were determined to be 5.3 ± 1.0 and 2.2 ± 0.5, respectively (Figure 1 (E)). The CN(Pt-Pt) decreased drastically from 9.6 to 5.3, which indicates the existence of both surface oxygen

and subsurface oxygen, forming a surface Pt²⁺O layer. [11,14,15] The observed Pt-O bond distance of 0.201 ±0.002 nm is similar to 0.200 nm for tetragonal PtO phase. By assuming a full coverage of tetragonal PtO phase at the Pt nanoparticle surface (Figure 1 (D)), the CN(Pt-Pt) and CN(Pt-O) values are estimated to be 5.7 and 2.4, respectively by eq.(4) and eq.(5).

$$\text{CN(Pt-Pt)} = \frac{12 \cdot (1^2 + 2^2 + 3^2)}{(1^2 + 2^2 + 3^2 + 4^2 + 5^2) + 9 \cdot 4^2} \\ (1^2 + 2^2 + 3^2 + 4^2 + 5^2) = 5.7 \quad (4)$$

$$\text{CN(Pt-O)} = \frac{5^2 \cdot 4 + 4^2 \cdot 2}{(1^2 + 2^2 + 3^2 + 4^2 + 5^2)} = 2.4 \quad (5)$$

These values well reproduce the observed CN values for Pt/C. The potential dependent surface structures at 0.4 V_{RHE} and 1.4 V_{RHE} are illustrated in Figure 1 (D).

The transient response series of *operando* time-resolved QXAFS–XRD for a Pt/C cathode catalyst in PEFC under the cyclic voltage processes 0.4 V_{RHE}→1.4 V_{RHE}→0.4 V_{RHE} (Figure 1 (C)) were analyzed as shown in Figure 2. The transient response curves of the white line peak height (proportional to Pt valence) (a and a'), CN(Pt-Pt) (b and b'), CN(Pt-O) (c and c'), integrated (111) peak intensity (d and d'), integrated (220) peak intensity (e and e') and Pt nanoparticle size estimated by the Scherrer's formula (f and f') of the MEA Pt/C catalyst in the voltage operations 0.4 V_{RHE}→1.4 V_{RHE} and 1.4 V_{RHE}→0.4 V_{RHE}, respectively are plotted against the reaction time in Figure 2.

The transient responses of the white line peak height, CN(Pt-Pt), CN(Pt-O), XRD (111) intensity, XRD (220) intensity and Pt metallic-phase size against the voltage operation 0.4 V_{RHE}→1.4 V_{RHE} were well fitted with the two exponential function (eq. (2)), respectively as shown by red curves in Figures 2 (a-f). The validity of the two component fittings is convinced from the comparison with the one component fittings.[21] The determined rate constants for the electronic and structural changes

and the change amounts are listed in Table 1. The rate constants thus obtained are not influenced by the Pt quantity and Pt utilization fraction in MEA but affected by the working state of active Pt nanoparticles in the MEA. This may be an advantage of the simultaneous QXAFS-XRD analysis of active catalyst itself over the macroscopic electrochemical analysis.

Figure 2 (a-f) reveals that the Pt nanoparticles in the Pt/C cathode catalyst under the transient voltage operation 0.4 V_{RHE}→1.4 V_{RHE} transform at the fast and slow successive steps with the rate constants k_1 and k_2 , respectively. The rate constants (k_1 and k_2) for the changes in Pt charging (valence increase), CN(Pt-Pt) and CN(Pt-O) were 1.20 s⁻¹ and 0.12 s⁻¹, 1.10 s⁻¹ and 0.13 s⁻¹, and 1.60 s⁻¹ and 0.15 s⁻¹, respectively. As for the rate constants (k_1 and k_2) for the changes in the integrated XRD (220) peak intensity and the Pt metallic-phase core size estimated from the XRD (220) peak, we first obtained the rate constants (k_1 and k_2) for the change in the integrated XRD (111) peak as 1.18 s⁻¹ and 0.14 s⁻¹, respectively, then these values were fixed to make fitting the transient profiles for the integrated XRD (220) peak intensity and Pt metallic-phase size to minimize the fitting error range because the XRD (220) peak is much weaker than the XRD (111) peak intensity and the rate constants for the changes in the three parameters should be identical. Thus, it is indicated that the dynamic behavior of the Pt surface under 0.4 V_{RHE}→1.4 V_{RHE} is initiated with the Pt-O bond formation ($k_{1(\text{Pt-O})} = 1.60 \text{ s}^{-1}$) (blue dotted line of Figure 3), followed by the Pt charging ($k_{1(\text{valence})} = 1.20 \text{ s}^{-1}$), metallic-phase size decrease ($k_{1(\text{XRD})} = 1.18 \text{ s}^{-1}$) and Pt-Pt bond dissociation ($k_{1(\text{Pt-Pt})} = 1.10 \text{ s}^{-1}$). The surface Pt-O bond formation event was followed by the decreases in the Pt metallic-phase size and CN(Pt-Pt) and the increase in the Pt valence. The

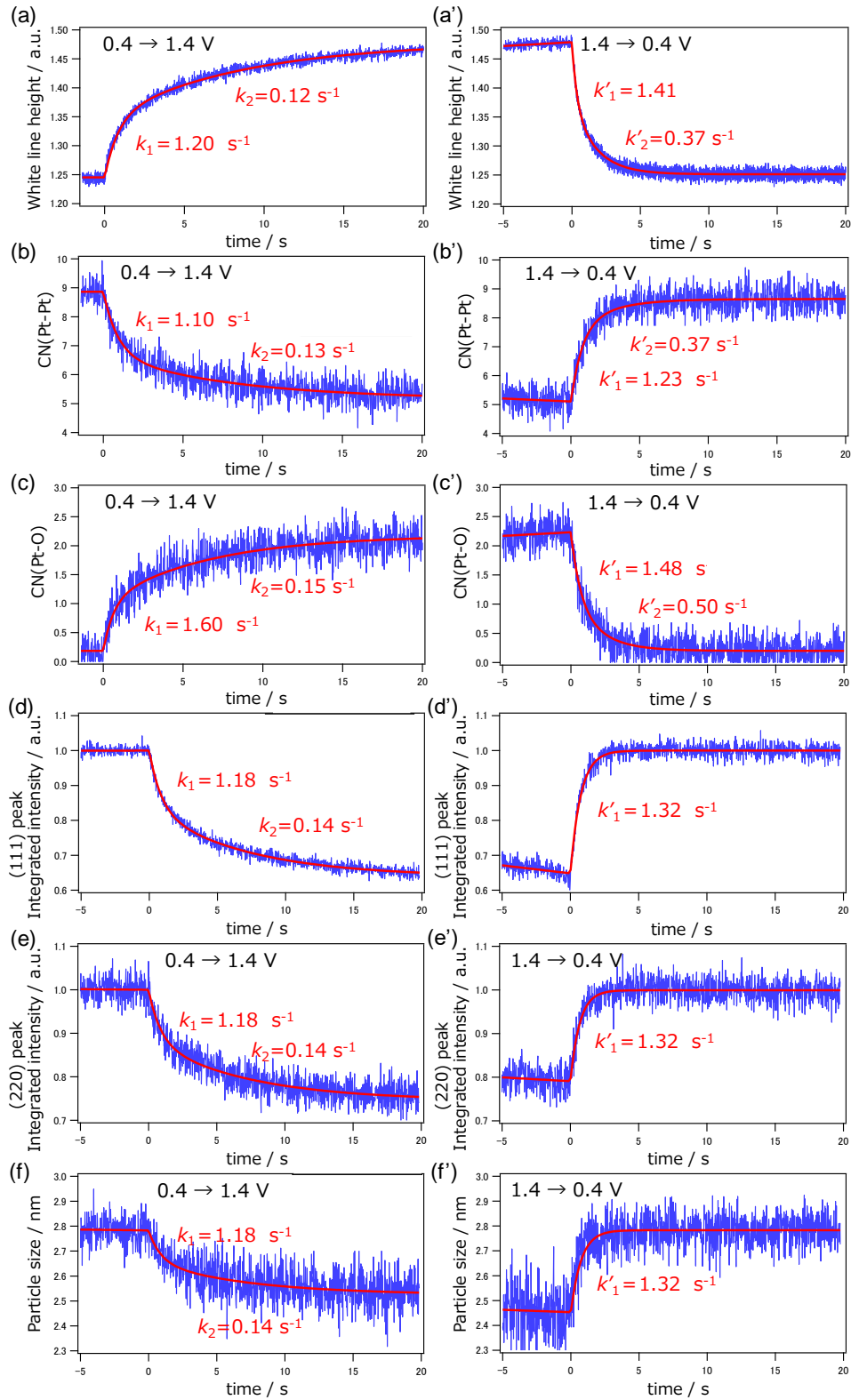


Figure 2. Transient response curves of the white line peak height (a and a'), CN(Pt-Pt) (b and b'), CN(Pt-O) (c and c'), integrated (111) peak intensity (d and d'), integrated (220) peak intensity (e and e') and Pt nanoparticle size (f and f') of the MEA Pt/C catalyst in the voltage operations 0.4 $V_{\text{RHE}} \rightarrow$ 1.4 V_{RHE} and 1.4 $V_{\text{RHE}} \rightarrow$ 0.4 V_{RHE} , respectively under H_2 (anode)– N_2 (cathode); Cell temp.: 353 K; Relative humidity: ~93%. Time resolution: 20 ms.

Table 1. Rate constants and change amounts

0.4→1.4 V	k_1 / s^{-1}	$a_1 / a.u.$	k_2 / s^{-1}	$a_2 / a.u.$	a_1 fraction / %	a_2 fraction / %
111 int	1.18±0.05	-0.16±0.00	0.14±0.01	-0.20±0.00	46±2	54±2
220 int	1.18 (fixed)	-0.12±0.00	0.14 (fixed)	-0.14±0.00	47±2	53±2
220 size	1.18 (fixed)	-0.14±0.00	0.14 (fixed)	-0.14±0.01	50±2	50±2
White line	1.20±0.05	0.10±0.00	0.12±0.00	0.13±0.00	43±2	57±2
CN _{Pt-Pt}	1.10±0.10	-2.1±0.1	0.13±0.01	-1.6±0.1	58±3	42±3
CN _{Pt-O}	1.60±0.20	0.83± 0.06	0.15±0.01	1.16±0.05	41±3	59±3
1.4→0.4 V	k'_1 / s^{-1}	$a'_1 / a.u.$	k'_2 / s^{-1}	$a'_2 / a.u.$	a'_1 fraction / %	a'_2 fraction / %
111 int	1.32±0.02	0.35±0.00	n.o.	n.o.	~100	~0
220 int	1.32 (fixed)	0.21±0.00	n.o.	n.o.	~100	~0
220 size	1.32 (fixed)	0.33±0.01	n.o.	n.o.	~100	~0
White line	1.41±0.32	-0.13±0.01	0.37±0.03	-0.10±0.01	57±4	43±4
CN _{Pt-Pt}	1.23±0.24	2.50±0.62	0.37±0.13	1.05±0.61	70±17	30±17
CN _{Pt-O}	1.48±0.44	-1.10±0.47	0.50±0.13	-0.93±0.46	54±23	46±23

n.o.: not observed. a_1 , a_2 , a'_1 and a'_2 fractions: $a_1/(a_1+a_2)$, $a_2/(a_1+a_2)$, $a'_1/(a'_1+a'_2)$ and $a'_2/(a'_1+a'_2)$, respectively.

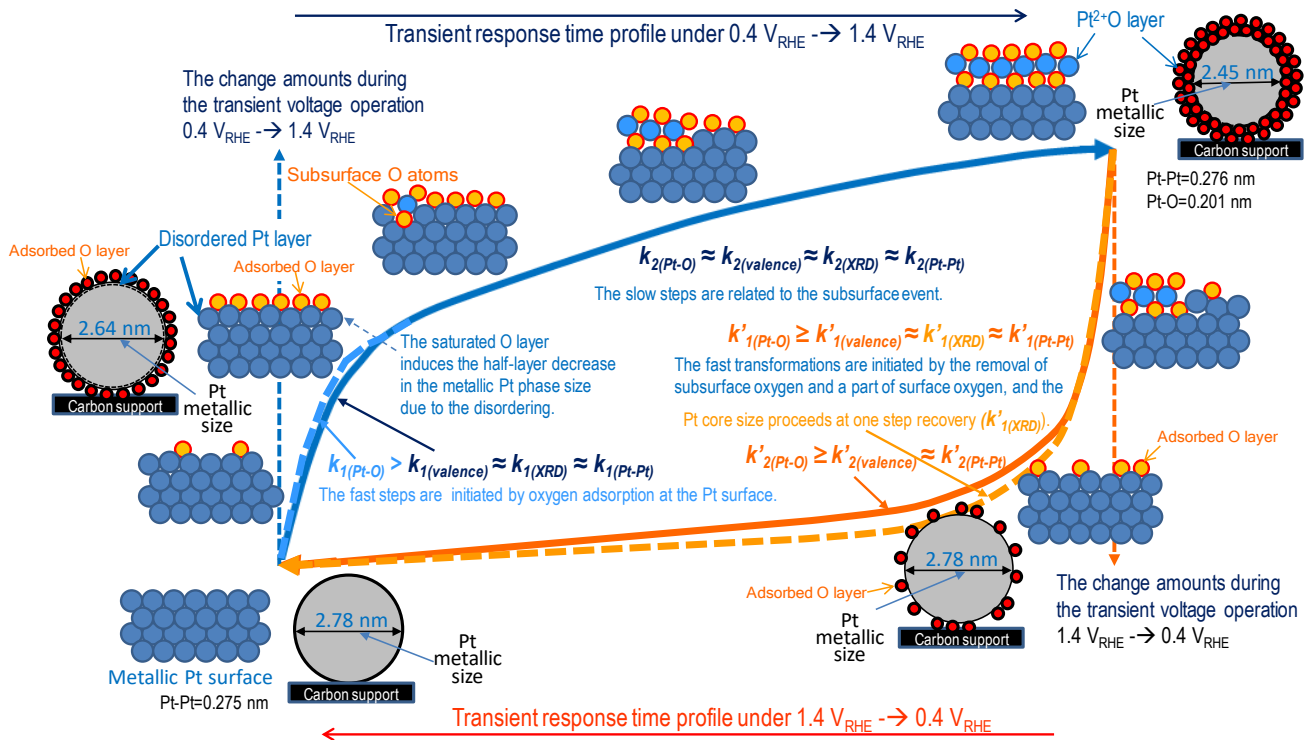


Figure 3. Reaction mechanism and structural kinetics for Pt surface events of an MEA Pt/C cathode catalyst under the transient cyclic voltage operations $0.4 V_{RHE} \rightarrow 1.4 V_{RHE} \rightarrow 0.4 V_{RHE}$. H_2 (anode)- N_2 (cathode); Cell temp.: 353 K; RH: ~93%. $k_{1(Pt-O)}$ & $k_{2(Pt-O)}$: Pt-O bond formation, $k_{1(valence)}$ & $k_{2(valence)}$: Pt charging, $k_{1(Pt-Pt)}$ & $k_{2(Pt-Pt)}$: Pt-Pt bond dissociation, and $k_{1(XRD)}$ & $k_{2(XRD)}$: Pt metallic-phase size decrease under $0.4 V_{RHE} \rightarrow 1.4 V_{RHE}$. $k'_{1(Pt-O)}$ & $k'_{2(Pt-O)}$: Pt-O bond dissociation, $k'_{1(valence)}$ & $k'_{2(valence)}$: Pt discharging, $k'_{1(Pt-Pt)}$ & $k'_{2(Pt-Pt)}$: Pt-Pt bond reformation, and $k'_{1(XRD)}$: Pt metallic-phase size increase under $1.4 V_{RHE} \rightarrow 0.4 V_{RHE}$.

results suggest that the surface Pt-O bond formation induces the partial disordering (rearrangement) of the outermost Pt layer, resulting in an apparent half-layer decrease in the metallic-phase size at the saturated O layer from 2.78 nm to 2.64 nm as shown in Figure 3.

The first fast surface event was followed by the second slow transformations of Pt-O bond formation, Pt charging, Pt-Pt bond dissociation and Pt metallic-phase size decrease; $k_{2(Pt-O)}=0.15 \text{ s}^{-1}$, $k_{2(valence)}=0.12 \text{ s}^{-1}$, $k_{2(Pt-Pt)}=0.13 \text{ s}^{-1}$, and $k_{2(XRD)}=0.14 \text{ s}^{-1}$ as shown in Table 1 and Figure 3. These rate constants are similar to each other within error ranges, which suggests that the slow Pt-O bond formation, Pt charging (valence increase), Pt-Pt bond dissociation and Pt metallic-phase size decrease occur concertedly to produce finally the tetragonal Pt²⁺O layer (Pt-O=0.201 nm) at the Pt surface (Figure 3). The slow steps involve the subsurface event. The metallic-phase core of the Pt nanoparticles decreases further from 2.64 nm to 2.45 nm (Figure 3).[21]

The amount changes (a_1 and a_2) in eq. (2) are also listed in Table 1. The a_1 fractions range 41-58% and the a_2 fractions range 42-59%, which indicates that the first step and second step constitute about 50%-50% event in the whole transformation.

The transient response time profiles under $1.4 V_{RHE} \rightarrow 0.4 V_{RHE}$ were also fitted by the two exponential function (eq.(2)) as shown in Figure 2 (a', b' and c'). The rate constants for the fast and slow transformation steps were determined to be $k'_{1(Pt-O)}=1.48 \text{ s}^{-1}$ and $k'_{2(Pt-O)}=0.50 \text{ s}^{-1}$ for Pt-O bond dissociation, $k'_{1(valence)}=1.41 \text{ s}^{-1}$ and $k'_{2(valence)}=0.37 \text{ s}^{-1}$ for Pt discharging, $k'_{1(Pt-Pt)}=1.23 \text{ s}^{-1}$ and $k'_{2(Pt-Pt)}=0.37 \text{ s}^{-1}$ for Pt-Pt bond reformation, respectively. The fitting result with the one-exponential function (eq.(1)) for the Pt valence change was not a good enough (not shown here), which reveals the validity of the two-

exponential functions fitting (Figure 2 (a')). In the cases of the CN(Pt-Pt) and CN(Pt-O) in Figure 2 (b' and c') the two-stage transformation (eq.(2)) was not definitely concluded by comparison with the one-exponential fitting by eq.(1) (one-wave fittings are not shown here), but the one-exponential fitting showed unreasonably small rate constants due to not good enough fitting at the beginning of the transient response curves. Further, the transformations under $0.4 V_{RHE} \rightarrow 1.4 V_{RHE}$ were well characterized by the two-stage (fast and slow) processes as shown in Figure 2 (a, b and c). Hence, we assumed that the reverse steps for the Pt-O and Pt-Pt event (Figure 2 (b' and c')) also proceed by two-stage transformations similar to the two-stage Pt valence change (Figure 2 a'). As the result, the first fast steps for the Pt-O bond dissociation (relaxation time: 0.67 s), Pt discharging (0.71 s) and Pt-Pt bond reformation (0.81 s) are suggested to occur at similar rates. In contrast to the QXAFS analysis, the transient response profiles of the XRD data (Figure 2 (d', e' and f')) were fitted with the one-exponential function (eq.(1)) and the fittings were not improved by the two- exponential functions. The rate constants for the increases in the integrated XRD (111) peak intensity, integrated XRD (220) peak intensity and metallic-phase core size under $1.4 V_{RHE} \rightarrow 0.4 V_{RHE}$ were determined as $k'_{1(XRD)}=1.32 \text{ s}^{-1}$ as shown in Figure 2 (d'-f'), Table 1 and Figure 3. In consequence, the Pt-O bond dissociation, Pt valence decrease, Pt-Pt bond reformation and Pt metallic-phase core size increase proceeds concertedly at the similar rates within experimental error range.

The second slow steps of Pt-O bond dissociation ($k'_{2(Pt-O)}=0.50 \pm 0.13 \text{ s}^{-1}$), Pt valence decrease ($k'_{2(valence)}=0.37 \pm 0.03 \text{ s}^{-1}$) and Pt-Pt bond reformation ($k'_{2(Pt-Pt)}=0.37 \pm 0.13 \text{ s}^{-1}$) under $1.4 V_{RHE} \rightarrow 0.4 V_{RHE}$ also occur concertedly. However, the XRD data for the integrated (111) peak intensity ($1.32 \pm 0.02 \text{ s}^{-1}$)

indicated a one-step event as shown by the one-wave fitting (Figure d'). The amount change (a_1' fraction) was 0.35 as shown in Table 1. The value coincides with the sum (0.36) of the a_1 and a_2 fractions under $0.4 V_{RHE} \rightarrow 1.4 V_{RHE}$ (Table 1). The a_1' fraction (0.33) for the increase in the Pt metallic-phase core size under $1.4 V_{RHE} \rightarrow 0.4 V_{RHE}$ was also similar to the sum (0.28) of the a_1 and a_2 fractions under $0.4 V_{RHE} \rightarrow 1.4 V_{RHE}$ (Table 1). These results suggest that the Pt metallic-phase core size increases in one step under $1.4 V_{RHE} \rightarrow 0.4 V_{RHE}$ unlike the two-stage decrease in the metallic-phase core size under $0.4 V_{RHE} \rightarrow 1.4 V_{RHE}$.

This may be explained as follows. The change amounts (a_1' fractions) of the first fast step for the Pt valence decrease, CN(Pt-O) decrease and CN(Pt-Pt) increase were 54-70% (av. 60%) of the total change amount. At this state there are no subsurface oxygen atoms at the surface layer of the Pt nanoparticles and the adsorbed oxygen coverage at the Pt surface is lower than the saturated one, where only a small partial disordering (small rearrangement) of the outermost Pt layer may occur, and as a result the surface oxygen gives almost no significant effect on the metallic-phase size. The change in the metallic-phase core size is completed at this stage as shown in Figure 3 (orange dotted line), and the change in the Pt valence, Pt-O bond dissociation and Pt-Pt bond reformation at the surface proceed further at the slower rates as shown in Figure 3 (orange solid line). Although the Pt/C cathode catalysis in PEFC for the ORR performance is reversible under the voltage operations $0.4 V_{RHE} \rightarrow 1.4 V_{RHE}$ and $1.4 V_{RHE} \rightarrow 0.4 V_{RHE}$, it is to be noted that the structural and electronic transformations and reaction kinetics for the eight elementary steps did not trace the similar transformations and kinetics in the forward and backward voltage operation processes and revealed

the different structural transformations and kinetics and the definite hysteresis as illustrated in Figure 3.

3.2 Relationships of the kinetic factors with the PEFC performance and durability.

The ORR activity and durability of the Pt/C cathode catalysts in PEFC may be related to the structural kinetics of the elementary reaction steps at the cathode Pt surface under the transient voltage operations, such as $k_{(valence)}$ and $k'_{(valence)}$, $k_{(Pt-O)}$ and $k'_{(Pt-O)}$, and $k_{(Pt-Pt)}$ and $k'_{(Pt-Pt)}$ under $0.4 V_{RHE} \rightarrow 1.4 V_{RHE}$ and $1.4 V_{RHE} \rightarrow 0.4 V_{RHE}$, respectively, which can be determined by *operando* time-resolved QXAFS, while measuring the electrochemical current/charge simultaneously.[11,14-17,26] The temporal variations in the electronic and structural parameters of the Pt/C (C: KB, AB and MWCNT) cathode catalysts in MEAs during the transient cycling voltage processes ($0.4 V_{RHE} \rightarrow 1.4 V_{RHE} \rightarrow 0.4 V_{RHE}$) under H_2 (anode) - N_2 (cathode) were investigated by *operando* time-resolved Pt L_{III}-edge QXAFS.[22] We found the structural kinetics (k'_{Pt-O} and $k'_{valence}$) controlling the oxygen reduction reaction (ORR) activity and also the structural kinetics (k'_{Pt-Pt}/k_{Pt-Pt}) reflecting the durability of the cathode catalysts as described below. The relaxation time of the Pt-Pt bond reformation and Pt-O bond dissociation processes in the activated MEAs was also suggested to predict the relative durability of the similar kinds of cathode catalysts.[22]

We plotted the analysis results on *operando* time-resolved QXAFS data for the PEFC Pt/C samples after accelerated durability test (ADT) by repeated triangle $1.0-1.5 V_{RHE}$ load treatments to examine the key issues for the long-term durability of PEFC Pt/C cathode catalysts in Figure 4.[22] However, the transient responses for the ADT samples were smaller than those for the activated Pt/C samples after aging treatment. Hence, we determined the rate

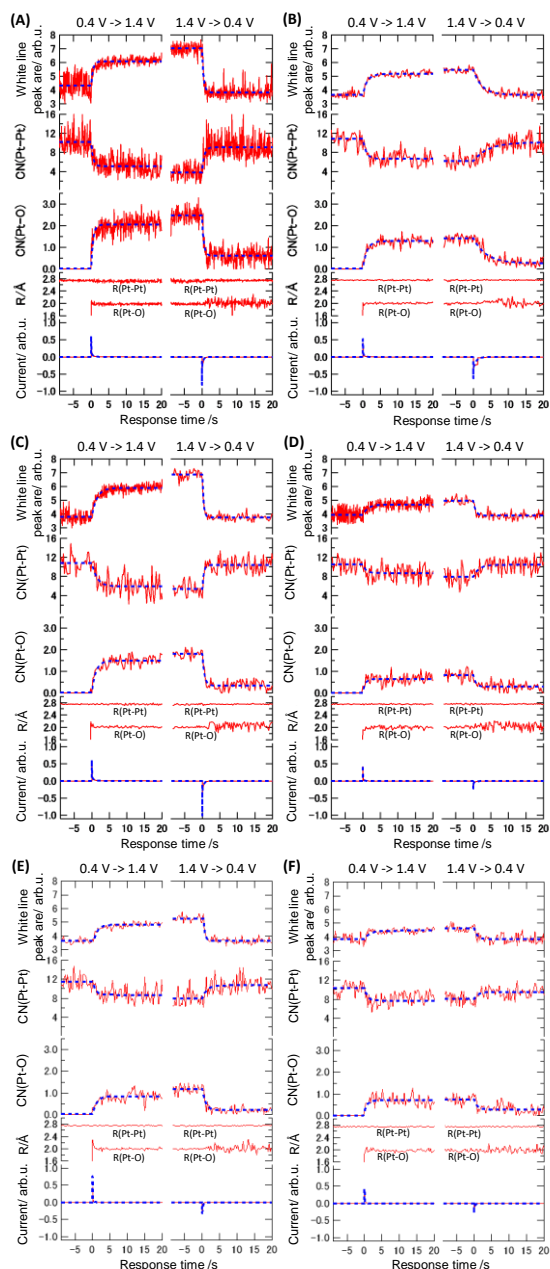


Figure 4. Transient response curves of the white line intensity, CN(Pt-Pt), CN(Pt-O), R(Pt-Pt), R(Pt-O), and current for Pt/KB after aging (A) and ADT 1000 cycles (B), Pt/AB after aging (C) and ADT 5000 cycles (D), and Pt/MWCNT after aging (E) and ADT 5000 cycles (F), under the voltage operations $0.4 V_{RHE} \rightarrow 1.4 V_{RHE}$ and $1.4 V_{RHE} \rightarrow 0.4 V_{RHE}$, respectively. H_2 (anode)- N_2 (cathode); Cell temp.: 353 K, RH: $\sim 93\%$. (A, C, E) every 100 ms; (B, D, F) every 300 ms. [Re.22]

constants for six elementary steps (Pt charging/discharging, Pt-O bond formation/

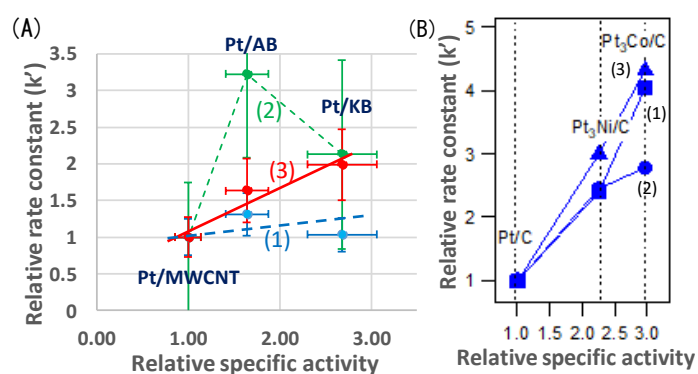


Figure 5. (A) Relationship between the rate constants ($k'_{valence}$ (1), k'_{Pt-Pt} (2) and k'_{Pt-O} (3) under $1.4 V_{RHE} \rightarrow 0.4 V_{RHE}$) and the relative surface specific activities for the Pt/KB, Pt/AB and Pt/MWCNT cathodes in the activated MEAs. [Ref.22] (B) Relationship between the rate constants ($k'_{valence}$ (1), k'_{Pt-O} (2) and k'_{Pt-Pt} (3) under $1.0 V_{RHE} \rightarrow 0.4 V_{RHE}$) and the relative surface specific activities for Pt/C, Pt_3Ni/C and Pt_3Co/C in the activated MEAs. [Ref.16,17]

dissociation and Pt-Pt bond dissociation/ reformation) by the one-exponential function (eq.(1)).

To find the structural kinetics of Pt/KB, Pt/AB and Pt/MWCNT in MEAs most relevant to the ORR activity (surface specific activity (SA)), the rate constants $k_{valence}$, $k'_{valence}$, k_{Pt-Pt} , k'_{Pt-Pt} , k_{Pt-O} , and k'_{Pt-O} , respectively for Pt charging and discharging, Pt-Pt bond dissociation and reformation, and Pt-O bond formation and dissociation were plotted against the SA in Figure 5 (A). The rate constants and the activities were referred to those for the Pt/MWCNT, respectively. The rate enhancements of the structural kinetics ($k_{valence}$, k_{Pt-Pt} and k_{Pt-O}) under the transient voltage operation ($0.4 V_{RHE} \rightarrow 1.4 V_{RHE}$) were not proportional to the ORR activity as reported previously.[22] The rate enhancement (k'_{Pt-Pt}) under the transient voltage operation ($1.4 V_{RHE} \rightarrow 0.4 V_{RHE}$) was not proportional to the ORR activity, either as shown in Figure 5 (A). Eventually, it was found that the rate enhancement (k'_{Pt-O}) in the Pt-O bond

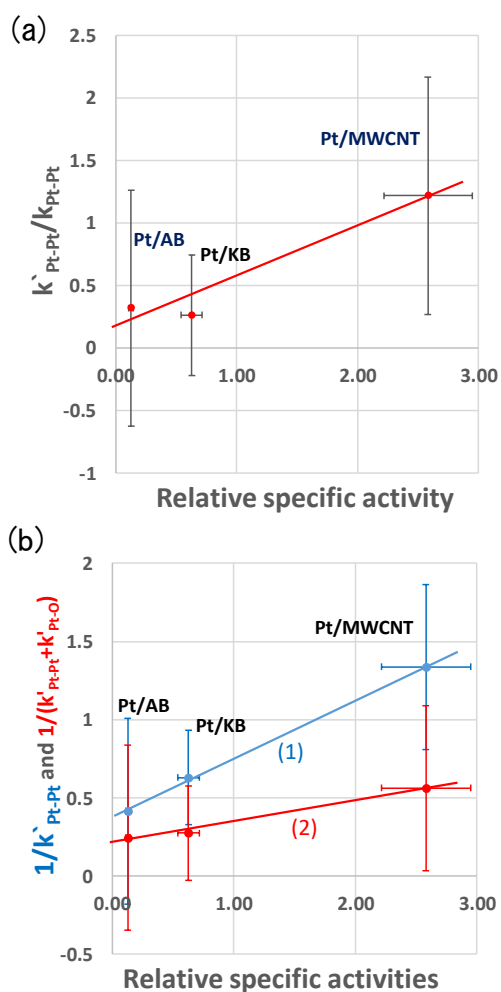


Figure 6. (a) Relationship between the relative surface specific activities and k'_{Pt-Pt}/k_{Pt-Pt} for the Pt/KB, Pt/AB and Pt/MWCNT cathodes in MEAs after the ADT cycles (Figure 4). The rate constants k_{Pt-Pt} and k'_{Pt-Pt} under $0.4 V_{RHE} \rightarrow 1.4 V_{RHE}$ and $1.4 V_{RHE} \rightarrow 0.4 V_{RHE}$, respectively for each sample after the ADT cycles are the relative values to those for each corresponding activated sample, respectively. (b) Relationship between the relative surface specific activities after the ADT cycles and $1/k'_{Pt-Pt}$ (1) or $1/(k'_{Pt-Pt} + k'_{Pt-O})$ (2) for the Pt/KB, Pt/AB and Pt/MWCNT cathodes in the activated MEAs. The rate constants k'_{Pt-Pt} and k'_{Pt-O} under $1.4 V_{RHE} \rightarrow 0.4 V_{RHE}$ are the values for each activated sample, respectively. The relative surface specific activities of each sample after the ADT cycles are the relative values to those of each corresponding activated sample. [Ref.22]

dissociation step under the transient voltage operation ($1.4 V_{RHE} \rightarrow 0.4 V_{RHE}$) showed the linear relationship with the SA (Figure 5 (A)). The blue dashed straight line was tentatively drawn to see the $k'_{valence}$ -activity relationship in Figure 5 (A). These aspects are similar to the alloy effect on the rate enhancement in the preceding work on Pt/C, Pt₃Co/C and Pt₃Ni/C by Tada et al. as shown in Figure 5 (B). [16,17] They evidenced the significant contribution of k'_{Pt-O} and k'_{valenc} to the PEFC activity by means of *in situ* time-resolved QXAFS.[16,17] The reduction of oxygen species from the Pt surface has also been demonstrated to be key steps in the ORR sequence.[30-32] The time-resolved QXAFS-transient response technique revealed that the ORR rate enhancement in PEFC is brought from the increase in the rate constants k'_{Pt-O} (main) and $k'_{valence}$, which depend on the kind of carbon support. The time-resolved QXAFS provides direct information on the key structural kinetics of the Pt/C catalysts.

Long-term durability of the MEA cathode catalysts may be a more serious issue for widely spread commercialization of PEFC vehicles. All rate constants were plotted against the SAs for the degraded Pt/KB, Pt/AB and Pt/MWCNT after the ADT cycles, but we could not find any relationship among them.[22] Only the ratio of two rate constants k'_{Pt-Pt}/k_{Pt-Pt} showed a linear relation with the cathode catalyst durability as shown in Figure 6 (a), where the rate constants k_{Pt-Pt} and k'_{Pt-Pt} for each degraded sample are the relative values to those for each corresponding activated sample after aging, respectively. The relative SA values of each degraded sample are also the relative values to those of each corresponding activated sample. The error range for the ratio k'/k is somewhat large due to a ratio, but the linear relationship in Figure 6 (a) was reproduced by different beamtime experiments at SPRing-8 BL36XU

(Subject numbers in 2015-2017 listed in Acknowledgement). The Pt/KB (ADT 1000 cycles), Pt/AB (ADT 5000 cycles) and Pt/MWCNT (ADT 5000 cycles), whose maximum power densities decreased to about 55-60% of the initial values, were used as the similarly degraded samples to explore the key factors for the durability of Pt nanoparticles on KB, AB and MWCNT. The ratio k'_{Pt-Pt}/k_{Pt-Pt} is a dimensionless quantity. The relative easiness of the recovery of an original metallic Pt surface at 0.4 V_{RHE} from the PtO layer at 1.4 V_{RHE} via the rough Pt surface, which is brought from the Pt-O bond dissociation, is regarded to correlate with the durability of the MEA Pt/C cathodes. It should be noted that the present estimation for the MEA durability is not the estimation of the speeds of the decreases in the rate constants and SAs as a function of the number of ADT cycles.

Next, we examined if we can predict the durability of the cathode catalysts in MEAs without durability tests for many hours. We found a good relationship between $1/k'_{Pt-Pt}$ (relaxation time) for the activated MEAs and the relative SA as shown in Figure 6 (b) (blue line (1)).[22] The k'_{Pt-Pt} is the rate constants for the Pt-Pt bond reformation in the activated Pt/KB, Pt/AB, and Pt/MWCNT under the transient voltage operation (1.4 V_{RHE} → 0.4 V_{RHE}), while the relative SAs of each sample are the relative values of the degraded samples to the activated samples. The larger the relaxation time for the Pt-Pt bond reformation, the longer the durability becomes. We also found a good relationship between $1/(k'_{Pt-Pt}+k'_{Pt-O})$ and the relative SA as shown in Figure 6 (b) (red line (2)).[22] A good linearity was not observed with the $1/k'_{Pt-O}$ alone, and hence the relaxation time of the Pt-Pt bond reformation rather than the Pt-O bond dissociation is more relevant to the durability. These results demonstrate that the Pt/MWCNT with the largest relaxation time for the Pt-Pt bond reformation

shows the highest durability. However, the Pt/MWCNT shows the lowest ORR activity due to the smallest k'_{Pt-O} among Pt/KB, Pt/AB and Pt/MWCNT as shown in Figure 4 (E) and Figure 5 (A). Materialization of decreasing the k'_{Pt-Pt} and increasing the k'_{Pt-O} simultaneously is demanded for improvements of both activity and durability of PEFC, but this may be a dilemma because the Pt-Pt bond reformation and Pt-O bond dissociation would not proceed independently. The whole behavior of PEFC performances during the triangular ADT cycles should be more complex, involving spatially heterogeneous carbon corrosion and Pt deterioration in MEA in addition to the structural kinetics of Pt nanoparticles.[33-35] Both time-resolved and spatially-resolved XAFS techniques may be powerful for understanding of the more detailed PEFC degradation. Further investigation is needed to confirm if the present approach and conclusion can be universally utilized in the development of PEFC cathode catalysts with high durability.

4. Conclusions

The simultaneous *operando* time-resolved QXAFS–XRD technique gained a new insight into the molecular-level reaction mechanism and key structural kinetics for the Pt/C electrocatalysis in PEFC under the transient cyclic voltage operations 0.4 V_{RHE}→1.4 V_{RHE}→ 0.4 V_{RHE} by determining the rate constants for eight elementary steps. A series of *operando* time-resolved QXAFS spectra for Pt/KB, Pt/AB, and Pt/MWCNT in PEFC under transient cyclic voltage operations was also investigated to find the relationship between the key structural kinetics and the SA and durability, which depended on the kind of carbon supports. The simultaneous *operando* time-resolved QXAFS–XRD technique is a promising technique which can aid the further understanding

and improvement of the PEFC performance and durability by providing the key material property and new insight and finding. (9)

ACKNOWLEDGEMENT. This work was supported by the New Energy and Industrial Technology Development Organization (NEDO) of the Ministry of Economy, Trade, and Industry (METI), Japan. XAFS measurements were conducted at BL36XU beamline in SPring-8 (No. 2013A7802, 2013B7806, 2014A7801, 2014A7805, 2014B7801, 2014B7803, 2014B7805, 2015A7803, 2015A7804, 2015A7840, 2015B7801, 2015B7803, 2015B7805, 2015B7840, 2016A7801, 2016A7802, 2016A7803, 2016A7840, 2016B7801, 2016B7803, 2016B7806, and 2016B7840, 2017A7801, 2017A7803, 2017A7806, 2017A7841).

References

- (1) L. Bu, N. Zhang, S. Guo, X. Zhang, J. Li, J. Yao, T. Wu, G. Lu, J.-Y. Ma, D. Su, X. Huang, *Science*, **354** (2016) 1410-1414.
- (2) H. Wang, S. Xu, C. Tsai, Y. Li, C. Liu, J. Zhao, Y. Liu, H. Yuan, *Science*, **354** (2016) 1031-1036. (16)
- (3) I. E. Stephens, A. S. Bondarenko, U. Grønbjerg, J. Rossmeisl, I. Chorkendorf, *Energy Environ. Sci.* **5** (2012) 6744-6762. (17)
- (4) K. Debe, *Nature*, **486** (2012) 43-51.
- (5) L. Zhang, L. T. Roling, X. Wang, M. V. Vara, M. Chi, J. Liu, S. Choi, J. Park, J. A. Herron, Z. Xie, *Science* **349** (2015) 412-416. (18)
- (6) M. Oezaslan, F. Hasché, P. Strasser, *J. Phys. Chem. Lett.* **4** (2013) 3273-3291. (19)
- (7) K. Nagasawa, S. Takao, S. Nagamatsu, G. Samjeské, O. Sekizawa, T. Kaneko, K. Higashi, T. Yamamoto, T. Uruga, Y. Iwasawa, *J. Am. Chem. Soc.* **137** (2015) 12856-12864. (20)
- (8) C. Chen, Y. Kang, Z. Huo, Z. Zhu, W. Huang, W. Huolin, L. Xin, J. D. Snyder, D. Li, J. A. Herron, *Science* **343** (2014) 1339-1343.
- R. Borup, J. Meyers, B. Pivovar, Y. S. Kim, R. Mukundan, N. Garland, D. Myers, M. Wilson, F. Garzon, D. Wood, *Chem. Rev.* **107** (2007) 3904-3951.
- V. R. Stamenkovic, B. Fowler, B. S. Mun, G. Wang, P. N. Ross, C. A. Lucas, N. M. Marcovic, *Science* **315** (2007) 493-497.
- M. Tada, T. Uruga, Y. Iwasawa, *Catal. Lett. (Silver Anniversary Special Issue)* **145** (2015) 58-70.
- S. Mukerjee, S. Srinivasan, M. P. Soriaga, J. McBreen, *J. Electrochem. Soc.* **142** (1995) 1409-1422.
- R. R. Adzic, J. X. Wang, B. M. Ocko, J. McBreen, *EXAFS, XANES, SXS. Handbook of Fuel Cells*; Wiley: Online, 2010.
- S. Nagamatsu, S. Takao, G. Samjeské, K. Nagasawa, O. Sekizawa, T. Kaneko, K. Higashi, T. Uruga, S. Gayen, S. Velaga, K. Milan, Y. Iwasawa, *Surf. Sci.* **648** (2016) 100-113.
- M. Tada, S. Murata, T. Asakoka, K. Hiroshima, K. Okumura, H. Tanida, T. Uruga, H. Nakanishi, S. Matsumoto, Y. Inada, M. Nomura, Y. Iwasawa, *Angew. Chem. Int. Ed.* **46** (2007) 4310.
- N. Ishiguro, S. Kityakarn, O. Sekizawa, T. Uruga, T. Sasabe, K. Nagasawa, T. Yokoyama, M. Tada, *J. Phys. Chem. C* **118** (2014) 15874-15883.
- N. Ishiguro, T. Saida, T. Uruga, O. Sekizawa, K. Nagasawa, K. Nitta, T. Yamamoto, S. Ohkoshi, T. Yokoyama, M. Tada, *Phys. Chem. Chem. Phys.* **15** (2013) 18827-18834.
- H. Imai, K. Izumi, M. Matsumoto, Y. Kubo, K. Kato, Y. Imai, *J. Am. Chem. Soc.* **131** (2009) 6293-6300.
- K.-W. Nam, S.-M. Bak, E. Hu, X. Yu, Y. Zhou, X. Wang, L. Wu, Y. Zhu, K.-Y. Chung, X.-Q. Yang, *Adv. Funct. Mater.* **23** (2013) 1047-1063.
- A. I. Frenkel, Q. Wang, N. Marinkovic, J. G. Chen, L. Barrio, R. Si, A. L. Cámara, A. M. Estrella, J. A. Rodriguez, J. C. Hanson, *J. Phys. Chem. C* **115** (2011)

- 17884–17890.
- (21) O. Sekizawa, T. Uruga, K. Higashi, T. Kaneko, Y. Yoshida, T. Sakata, and Y. Iwasawa, *ACS Sus. Chem. Eng.* **5** (2017) 3631–3636.
- (22) T. Kaneko, G. Samjeské, S. Nagamatsu, K. Higashi, O. Sekizawa, S. Takao, T. Yamamoto, X. Zhao, T. Sakata, T. Uruga, and Y. Iwasawa, *J. Phys. Chem. C*, **120** (2016) 24250–24264.
- (23) K. Nagasawa, S. Takao, K. Higashi, S. Nagamatsu, G. Samjeské, Y. Imaizumi, O. Sekizawa, T. Yamamoto, T. Uruga, Y. Iwasawa, *Phys. Chem. Chem. Phys.* **16** (2014) 10075–10087.
- (24) O. Sekizawa, T. Uruga, M. Tada, K. Nitta, K., Kato, H. Tanida, K. Takeshita, S. Takahashi, M. Sano, H. Aoyagi, A. Watanabe, N. Nariyama, H. Ohashi, H. Yumoto, T. Koyama, Y. Senba, T. Takeuchi, Y. Furukawa, T. Ohata, T. Matsushita, Y. Ishizawa, T. Kudo, H. Kimura, H. Yamazaki, T. Tanaka, T. Bizen, T. Seike, S. Goto, H. Ohno, M., Takata, H. Kitamura, T. Ishikawa, T. Yokoyama, Y. Iwasawa, *J. Phys. Conf. Ser.* **430** (2013) 012020-1.
- (25) Y. Iwasawa, *X-ray Absorption Fine Structure for Catalysts and Surfaces*; World Scientific Publishing: Singapore, 1996.
- (26) Y. Iwasawa, K. Asakura, M. Tada, *XAFS Techniques for Catalysts, Nanomaterials and Surfaces*; Springer: New York, 2016.
- (27) M. Newville, B. Ravel, D. Haskel, J. J. Rehr, E. A. Stern, Y. Yacoby, *Phys. B* **208–209** (1995)154–156.
- (28) B. Ravel, M. Newville, ATHENA, ARTEMIS, HEPHAESTUS: Data Analysis for X-ray Absorption Spectroscopy Using IFEFFIT. *J. Synchrotron Rad.* **12** (2005) 537-541.
- (29) J. J. Rehr, R. C. Albers, *Rev. Mod. Phys.* **72** (2000) 621-654
- (30) V. R. Stamenkovic, B. Fowler, B. S. Mun, G. Wang, P. N. Ross, C. A. Lucas, N. M. Marcovic, *Science* **315** (2007) 493–497.
- (31) P. Hirunsit, P. B. Balbuena, *Surf. Sci.*, **603** (2009) 3239-3248.
- (32) I. Matanovic, F. H. Garzon, N. J. Henson, *J. Phys. Chem. C*, **115** (2011) 10640-10650.
- (33) S. Takao, O. Sekizawa, S. Nagamatsu, T. Kaneko, T. Yamamoto, G. Samjeské, K. Higashi, K. Nagasawa, T. Tsuji, M. Suzuki, N. Kawamura, M. Mizumaki, T. Uruga, Y. Iwasawa, *Angew. Chem. Int. Ed.* **53** (2014) 14110.
- (34) S. Takao, O. Sekizawa, G. Samjeské, S. Nagamatsu, T. Kaneko, T. Yamamoto, K. Higashi, K. Nagasawa, T. Uruga, Y. Iwasawa, *J. Phys. Chem. Lett.* **6** (2015) 2121.
- (35) S. Takao, O. Sekizawa, G. Samjeské, S. Namagatsu, T. Kaneko, K. Higashi, T. Yamamoto, K. Nagasawa, X. Zhao, T. Uruga, and Y. Iwasawa, *Topics Catal. (ISHHC17 issue)*, **59** (2016) 1722-1731.